

OPTIMIZED WEIGHTED ESSENTIALLY NON-OSCILLATORY SCHEMES FOR COMPUTATIONAL AEROACOUSTICS

Z.J. Wang*

Department of Mechanical Engineering
Michigan State University, East Lansing, MI 48804
and

R. F. Chen⁺

DaimlerChrysler Corporation, Auburn Hills, MI 48083

Abstract

ENO (Essentially Non-Oscillatory) and weighted ENO (WENO) schemes were designed for high-resolution of discontinuities such as shock waves. They are uniformly high-order accurate, and essentially oscillation free. Optimized schemes such as the DRP (Dispersion-Relation-Preserving) schemes are optimized for short waves (with respect to the grid spacing Δx , e.g., waves that are $6-8\Delta x$ in wave length) in the wave number space. Although they may have formally lower order accuracy than non-optimized maximum-order schemes, they are capable of resolving short waves with higher accuracy. Therefore, they are better suited for broadband acoustic wave problems. In this paper, we seek to unite the advantages of ENO, WENO schemes and optimized schemes through the development of Optimized Weighted ENO (OWENO) schemes to tackle shock/broadband acoustic wave interactions and small scale flow turbulences relative to the grid spacing. A third-order OWENO and a seventh order WENO scheme are compared against each other for performance on the scalar model equation. It has been shown that the OWENO scheme indeed gives much better results in resolving short waves than the WENO scheme while yielding non-oscillatory solutions for discontinuities. The OWENO scheme is then extended to the linearized Euler equations to solve two computational aeroacoustics (CAA) benchmark problems for which analytical solutions are available. For both cases, excellent agreement with analytical solutions has been achieved.

Introduction

The last one and half decade has seen many impressive development in computational aeroacoustics (CAA). As pointed out by Tam [20], aeroacoustic problems differ significantly from the aerodynamic problems in nature, characteristics, and objectives. They are intrinsically unsteady, and the dominant frequencies are usually high. Therefore the development of CAA algorithms needs independent thinking. As a result of this independent thinking, many powerful numerical algorithms have been developed to address the particular problems in CAA, e.g., the Dispersion-Relation-Preserving (DRP) finite difference schemes [21] and other

high-order algorithms [6, 9, 11, 14, 17]. The basic idea in DRP schemes is to optimize the scheme coefficients for the high-resolution of short waves with respect to the computational grid i.e., waves with wavelength of $6-8\Delta x$ (defined here as 6-8 points-per-wave or PPW). Therefore, DRP schemes are also called optimized schemes. The idea of optimizing the scheme coefficients to minimize a particular type of error instead of the truncation error has been used very successfully over the years by many researchers in designing a variety of optimized schemes [3, 10, 13, 24]. The rationale for optimizing numerical schemes for short waves is that in a broadband acoustic wave, there are both short and long wave components (relative to the grid spacing). For long waves, even lower-order schemes can do a decent job in resolving them. It is the short waves, however, which require high resolution if one is to resolve the broadband wave with as high accuracy as possible. Other optimized schemes have also been developed successfully for CAA applications [25-27]. In the DRP schemes, central differences are employed to approximate the first derivative. They are, therefore, non-dissipative in nature. Although non-dissipative schemes are ideal for aeroacoustic problems, numerical dissipations are required to damp any non-physical waves generated by boundary and/or initial conditions. In practice, high-order dissipation terms are added to the DRP schemes to suppress spurious oscillations. The amount of artificial dissipations required is, however, problem dependent. One may need to fine tune the artificial damping to obtain the best results for a particular problem at hand. To remedy this problem, optimized upwind DRP schemes have been developed more recently by Zhuang and Chen [25,26]. Instead of using the central difference stencil, an upwind-biased stencil was selected based on the local wave propagating direction. Then the upwind schemes are optimized in the wave-number space following the same idea of DRP schemes. The upwind DRP schemes are by design dissipative. Therefore they are capable of suppressing spurious oscillations without the addition of extra artificial damping, relieving the user from fine tuning the amount of numerical dissipations. Another advantage of the upwind DRP schemes is that acceptable results can be obtained even if the mean flow contains discontinuities. With both the DRP and upwind DRP schemes, it is very difficult to obtain oscillation-free numerical solutions

*Associate Professor, Member AIAA, zjw@egr.msu.edu

⁺Project Engineer, Member AIAA, rc171@daimlerchrysler.com

Copyright 2001 by Z.J. Wang and R.F. Chen. Published by AIAA Inc. with permission

if the mean flow is discontinuous because the schemes are linear. For non-linear shock-acoustic wave interaction problems, numerical oscillations may contaminate the resultant solutions and even diverge the simulations.

ENO (Essentially Non-Oscillatory) schemes started with the classic paper of Harten, Engquist, Osher and Chakravarthy in 1987 [5]. It is well-known that traditional finite difference schemes use fixed stencils to construct a high-order data interpolation or approximate the first derivative. The resultant schemes are linear for linear partial differential equations. These schemes can usually achieve their formal order of accuracy if the solution is globally smooth. For problems with discontinuities such as shock waves or contact discontinuities, fixed stencil high-order (second-order or higher) schemes are necessarily oscillatory near a discontinuity. Furthermore, such oscillations do not decay in magnitude when the mesh is refined. These oscillations can often break down a simulation for non-linear problems containing discontinuities. To suppress numerical oscillations, several approaches are possible. One approach is to add artificial dissipations [7]. The dissipations can be tuned to be large enough near discontinuities to suppress oscillations, but small elsewhere to maintain high-order accuracy. A disadvantage of the approach is that the dissipation terms are problem dependent. Another approach is to use limiters to eliminate oscillations [23]. The popular TVD schemes [4, 15] are just such examples. One drawback of this approach is that the accuracy near extrema (even near smooth extrema) must degrade to first order, resulting in clipping of smooth extrema. The ENO idea seems to be the first successful attempt to obtain a self similar (i.e. no mesh size dependent parameter), uniformly high-order accurate, yet essentially non-oscillatory interpolation (i.e the magnitude of the oscillations decays as $O(\Delta x^k)$ where k is the order of accuracy) for piecewise smooth functions. More recently, weighted ENO (WENO) schemes [8, 12, 19] were developed to further increase the order of accuracy, while resolving discontinuities with essentially no numerical oscillations. Many studies [1, 2] confirmed that ENO and WENO schemes are indeed uniformly high-order accurate, and resolve shocks with high resolution. They have been successfully applied to problems with shocks and complex smooth flow structures, such as those occurring in shock interactions with a turbulent flow, and shock/vortices interactions. Although ENO schemes are not designed for CAA, they have been applied to CAA problems because of their high-order of accuracy. The direct applications of ENO and WENO to CAA problems are, however, not optimum because ENO and WENO schemes are designed for high-resolution of discontinuities and to achieve a high formal order of accuracy, and NOT optimized for broadband acoustic waves. For short waves, ENO and WENO schemes suffer the same drawback of conventional maximum-order finite difference schemes in that they quickly lose resolution

compared to optimized schemes.

In this study, we seek to unite the advantages of both the optimized DRP schemes and WENO schemes in the development of Optimized WENO (OWENO) schemes. The idea is to optimize the WENO schemes in the wave number space following the practice of the DRP schemes to achieve high-resolution for short waves with about 6 PPW. At the same time, OWENO schemes will retain the advantages of WENO schemes in that discontinuities are captured with essentially no oscillations, and without any extra numerical damping. Therefore, OWENO schemes will perform as well as WENO schemes near discontinuities while having the advantage of the optimized schemes of resolving broadband noise elsewhere. At least one group of researchers [24] attempted to optimize WENO schemes for short waves. In the approach presented in [24] only the weights in the WENO schemes are optimized. Although it was also found in [24] that the smoothness indicators added significant numerical dampings for short waves, no solutions were given there. In this study, optimizations are done in two levels. In the first level, optimized schemes for all candidate stencils are constructed. In the second level, optimizations are also performed to find the best weights to combine all the stencils. In addition, new smoothness indicators are presented for short waves. In the following section, we first review the concept behind optimized schemes, ENO and WENO schemes. Then OWENO schemes are derived for the linear wave equation, and their dissipative and dispersive behaviors analyzed. After that, the extension of OWENO to the linear Euler equations is described followed by a brief discussion on the time marching method. Next, sample demonstration cases with 1D scalar wave equation, and the linearized Euler equations are carried out to evaluate the performance of OWENO schemes. Finally conclusions from the study are summarized, and possible future work is outlined.

Overview of Optimized, ENO and WENO Schemes

Given the number of grid points used to construct a finite difference scheme, the usual practice is to maximize the order of accuracy of the numerical scheme. For example, if seven points are used to build a finite difference scheme, the maximum order of accuracy one can achieve is a sixth-order scheme. However, maximum-order schemes may not be the best for high-frequency short waves. In order to resolve high-frequency short waves, one can optimize the coefficients of the finite difference scheme for a particular range of wave number. This is exactly the idea developed in the DRP schemes [21]. Consider the scalar wave equation with a constant positive wave speed a :

$$\frac{\partial u}{\partial t} + a \frac{\partial u}{\partial x} = 0 \quad (1)$$

where u is a state variable, $t > 0$ is time, and x is the Cartesian coordinate. We assume proper initial and boundary conditions are available when necessary. Given a uniform grid

$$x_0 < x_1 < \dots < x_N \quad (2)$$

with a constant grid spacing Δx , we seek to develop a semi-discrete conservative numerical scheme approximating (1) in the following form:

$$\frac{\partial u_i}{\partial t} + \frac{a}{\Delta x}(\tilde{u}_{i+1/2}^r - \tilde{u}_{i-1/2}^r) = 0 \quad (3)$$

where u_i is a numerical approximation to $u(x, t)$ at grid point x_i , $\tilde{u}_{i+1/2}^r$ and $\tilde{u}_{i-1/2}^r$ are numerical fluxes (more precisely $a\tilde{u}_{i+1/2}^r$ is the flux) depending on k continuous grid points including x_i itself, i.e.,

$$\tilde{u}_{i+1/2}^r = \tilde{u}_{i+1/2}^r(u_{i-r}, \dots, u_{i+s}) = \sum_{j=0}^{k-1} c_{rj} u_{i-r+j}. \quad (4)$$

Here $r \geq 0$, $s \geq 0$, and $r + s + 1 = k$, k is the size of the stencil used to compute the numerical flux, and c_{rj} are constants independent of the solution. Note that the numerical scheme (3) also has a stencil size, which is $k+1$. In this paper, when we refer to the *size of the stencil*, we always refer to the stencil used to compute the numerical flux. In (4), the superscript r emphasizes the fact that there are r points to the left side of x_i in the stencil when we compute the numerical flux. The coefficients c_{rj} can be determined through a Taylor expansion to achieve a maximum k th order accuracy, i.e., by satisfying

$$\frac{\partial u_i}{\partial x} = \frac{(\tilde{u}_{i+1/2}^r - \tilde{u}_{i-1/2}^r)}{\Delta x} + O(\Delta x^k) \quad (5)$$

where $\frac{\partial u_i}{\partial x}$ is a shorthand for $\left. \frac{\partial u}{\partial x} \right|_{x_i}$. The Taylor expansion would yield the following equation:

$$(\tilde{u}_{i+1/2}^r - \tilde{u}_{i-1/2}^r) = \sum_{j=1}^k \varphi_j \frac{\partial^j u_i}{\partial x^j} \Delta x^j + O(\Delta x^{k+1}) \quad (6)$$

To satisfy (6), the following k equations must hold

$$\begin{aligned} \varphi_1 &= 1 \\ \varphi_j &= 0, \text{ for } j = 2, \dots, k \end{aligned} \quad (7)$$

These equations will give a unique solution for the coefficients c_{rj} in (4). For example, if $r = 2$, $s = 3$, a sixth order scheme is obtained with the following coefficients:

$$\begin{aligned} c_{20} &= 1/60, c_{21} = -2/15, c_{22} = 37/60, c_{23} = 37/60, c_{24} = -2/15, \\ c_{25} &= 1/60 \end{aligned} \quad (8)$$

The philosophy of optimized schemes is to sacrifice the formal order of accuracy for achieving better resolution for a wider range of wavenumbers, and for short waves in particular. Instead of always achieving the maximum order of accuracy of k , we set to design a scheme with formal order of accuracy of

p_I with $p_I < k$, i.e.,

$$\frac{\partial u_i}{\partial x} = \frac{(\tilde{u}_{i+1/2}^r - \tilde{u}_{i-1/2}^r)}{\Delta x} + O(\Delta x^{p_I}) \quad (9)$$

Similarly using a Taylor expansion, we can derive p_I equations about the coefficients c_{rj} . We need an extra $k - p_I$ equations to determine all the coefficients.

It is well-known that (1) has the following analytical solution

$$u(x, t) = U_0 \exp[\sqrt{-1}\alpha(x - at)] \quad (10)$$

if the initial condition is given by

$$u(x, 0) = U_0 \exp(\sqrt{-1}\alpha x) \quad (11)$$

where α is the spatial wavenumber. Assuming a solution in the form

$$u(x, t) = v(t) \exp(\sqrt{-1}\alpha x) \quad (12)$$

and substituting it into (3), we obtain the following ordinary differential equation

$$\frac{\partial v}{\partial t} = -\sqrt{-1}a\bar{\alpha}v \quad (13)$$

where $\bar{\alpha}$ is called the numerical wavenumber for the numerical scheme, which is dependent on the spatial difference operator. The numerical wavenumber for (3) with the given stencil can be found to be

$$\bar{\alpha}^r \equiv \frac{-\sqrt{-1}}{\Delta x} \sum_{j=-r}^s c_{r,j+r} \exp(\sqrt{-1}j\alpha\Delta x) [1 - \exp(-\sqrt{-1}\alpha\Delta x)] \quad (14)$$

It is argued [21] that if the numerical wave number is close to the exact wave number for a range of wave numbers, the numerical scheme would have high resolution for waves in the wave number range. Therefore, the optimization problem is to minimize the L_2 norm of the difference between the numerical wavenumber and the actual wave number for a particular wave number range $[-\alpha_0\Delta x, \alpha_0\Delta x]$. To be more specific, we seek c_{rj} so that they satisfy equation (9) and minimize the following integral

$$E_r = \int_{-\alpha_0\Delta x}^{\alpha_0\Delta x} \{ \lambda [\text{Re}(\bar{\alpha}^r \Delta x) - \alpha \Delta x]^2 + (1 - \lambda) [\text{Im}(\bar{\alpha}^r \Delta x)]^2 \} d(\alpha \Delta x) / 5$$

where E_r is the error to be minimized, parameter λ is chosen to be between 0 and 1 to balance the errors in the real and the imaginary parts. The imaginary part is a measure of the amplitude error, while the real part indicates the phase error. If the imaginary part is positive, the wave is a growing one in amplitude, indicating instability. For a non-dissipative central difference scheme, the imaginary part of the numerical wavenumber diminishes, and the minimization problem is simplified. Interested readers should refer to [21] for more information on the central DRP schemes. For upwind optimized schemes, refer to [25, 26] for details.

The design philosophy for ENO schemes [5] is very much different from that for the optimized schemes. ENO schemes were developed primary for high-accuracy capturing of discontinuities or steep gradients. This was achieved through “adaptive stencil”, namely to change the left shift r with the location x_i depending on the smoothness of the local solution. Given the current grid point x_i and a fixed order of accuracy k , it is seen that there are k possible candidate stencils $\{x_{i-r}, \dots, x_{i+s}\}$ for $r = 0, 1, \dots, k-1$. The “smoothest” stencil among all the possible stencils is then chosen to be the ENO stencil. After that the coefficients c_{rj} in this stencil are solely determined by maximizing the order of accuracy. The most widely used approach in selecting the smoothest stencil is to use the Newton divided or undivided differences as the smoothness indicators. Given any function $V(x)$, the 0 -th degree divided difference of the function $V(x)$ is defined by

$$V[x_i] = V(x_i) \quad (16)$$

and in general the j -th degree divided differences, for $j > 1$ are defined inductively by

$$V[x_i, \dots, x_{i+j}] = \frac{V[x_{i+1}, \dots, x_{i+j}] - V[x_i, \dots, x_{i+j-1}]}{\Delta x} \quad (17)$$

The process of picking the ENO stencil starts with the current point x_i , i.e.,

$$S(i) = \{x_i\} \quad (18)$$

Then the next point is picked from the point to the left and to the right of the current stencil. Therefore, we have two new candidate stencils to pick from, i.e., $\{x_{i-1}, x_i\}$ and $\{x_i, x_{i+1}\}$. The divided differences are used as the selection criterion. If

$$|V[x_i, x_{i+1}]| > |V[x_{i-1}, x_i]| \quad (19)$$

the stencil $\{x_{i-1}, x_i\}$ is selected. Otherwise, the stencil $\{x_i, x_{i+1}\}$ is chosen. This process is carried out recursively until the stencil size reaches k . Once the stencil is decided, the coefficients c_{rj} are used to construct a maximum order scheme on the selected stencil.

Note that in selecting the ENO stencil of k points, the field data at $2k-1$ points is scanned. If one uses all the data scanned in the selection process, one can achieve a maximum $(2k-1)$ -th order of accuracy if the solution on the $2k-1$ points is smooth. This is exactly the idea used in the WENO schemes. Instead of using only one of the candidate stencils to form the numerical flux, one uses a convex combination of all of them. To be more specific, suppose the k candidate stencils

$$S_r(i) = \{x_{i-r}, \dots, x_{i+s}\}, \quad r = 0, \dots, k-1 \quad (20)$$

produce k different reconstructions $\tilde{u}_{i+1/2}^r$, $r = 0, \dots, k-1$. The WENO reconstruction would take a convex combination of all $\tilde{u}_{i+1/2}^r$ as a new approximate to the flux formula, i.e.,

$$\tilde{u}_{i+1/2} = \sum_{r=0}^{k-1} d_r \tilde{u}_{i+1/2}^r \quad (21)$$

where d_r are the weights. Apparently the key to the success of WENO schemes would be the choice of the weights d_r . The following conditions must be satisfied for consistency and stability:

$$d_r \geq 0, \quad \text{and} \quad \sum_{r=0}^{k-1} d_r = 1 \quad (22)$$

If the solution is smooth in all the candidate stencils, there exist unique constants d_r such that

$$\frac{\partial u_i}{\partial x} = \frac{(\tilde{u}_{i+1/2} - \tilde{u}_{i-1/2})}{\Delta x} + O(\Delta x^{2k-1}) \quad (23)$$

These weights, however, cannot be used if there is a discontinuity in one of the stencils. Therefore, we wish to turn off the contributions made by the stencils with at least one discontinuity. Following [8], the following weights can be used

$$w_r = \frac{\delta_r}{\sum_{r=0}^{k-1} \delta_r}, \quad \delta_r = \frac{d_r}{(\varepsilon + \beta_r)^2}$$

$$\beta_r = \sum_{l=1}^{k-1} \int_{x_{i-1/2}}^{x_{i+1/2}} \Delta x^{2l-1} \left(\frac{\partial^l p_r(x)}{\partial^l x} \right)^2 dx, \quad r = 0, \dots, k-1 \quad (24)$$

where $p_r(x)$ is the *constructed* polynomial of $(k-1)$ th order over the interval $[x_{i-1/2}, x_{i+1/2}]$ determined by the given solutions on stencil $\{x_{i-r}, \dots, x_{i+s}\}$ assuming they represent cell-averaged quantities, ε is a small number preventing the denominator to be zero, and β_r is the smoothness indicator. The smoothness indicators for $k = 2, 3$ are given in [8, 19], and the indicators for $k = 4 - 6$ are given in [1]. Note that common factors are omitted in the indicators given in [1] for computational efficiency.

Optimized WENO Schemes

With the descriptions on optimized schemes, ENO and WENO schemes, it is then straightforward to present the OWENO schemes. The OWENO schemes are developed in the following two major steps.

Step 1. Given the stencil size k , develop optimized schemes achieving p_l -th order of accuracy ($p_l \leq k$) for all the k candidate stencils

$$\{x_{i-r}, \dots, x_{i+k-r-1}\}, \quad r = 0, 1, \dots, k-1. \quad (25)$$

By satisfying (9), p_l linear equations of the following form can be obtained about c_{rj}

$$\sum_{j=0}^{k-1} b_{lj} c_{rj} = z_l, \quad \text{for } l = 1, \dots, p_l \quad (26)$$

where b_{lj} and z_l are constants. The rest of the $k - p_l$ free

parameters are determined by minimizing the difference between the numerical wavenumber and the actual wave number over a specified range of wavenumber, i.e., by minimizing E_r in (15). E_r is a function of the coefficients c_{rj} ,

$$E_r = E_r(c_{r0}, \dots, c_{r,k-1}) \quad (27)$$

Equations (26) can be used to eliminate p_l coefficients. Without loss of generality, we assume that the first p_l coefficients c_{rj} , $j = 0, p_l - 1$ are eliminated, and they can be expressed as functions of the last $k - p_l$ parameters. Substitute these expressions into (27), we obtain:

$$E_r = E_r(c_{r,p_l}, \dots, c_{r,k-1}) \quad (28)$$

To minimize E_r , the following conditions must be satisfied

$$\frac{\partial E_r}{\partial c_{rj}} = 0, \quad \text{for } j = p_l, \dots, k-1 \quad (29)$$

Equations (29) would give the desired solution for the remaining coefficients.

Step 2. These optimized schemes for all the k candidate stencils are then convexly combined to obtain the OWENO schemes. The weights used in OWENO schemes, however, are not only constructed to achieve higher order of accuracy in smooth regions as in the WENO schemes but also to minimize the numerical error in the wave number space. Following WENO schemes, smoothness indicators are also built in the weights so that the stencils containing at least a discontinuity essentially do not contribute to the OWENO scheme, emulating the successful ENO idea. More specifically, we first seek constants h_r in the combination $\tilde{u}_{i+1/2} = \sum_{r=0}^{k-1} h_r \tilde{u}_{i+1/2}^r$ so that if the solution is smooth over all candidate stencils, we have

$$\frac{1}{\Delta x} (\tilde{u}_{i+1/2} - \tilde{u}_{i-1/2}) = \left(\frac{\partial u}{\partial x} \right)_i + O(\Delta x^{p_1+p_2}) \quad (30)$$

with $\sum_{r=0}^{k-1} h_r = 1$, $h_r \geq 0$ and $p_2 \leq k - 1$. Equation (30) can be used to determine p_2 weights, leaving $k - 1 - p_2$ weights as free parameters. These free parameters can then again be determined by minimizing an integral in the form of equation (15), but with $\bar{\alpha}^r$ replaced by $\bar{\alpha} = \sum_{r=0}^{k-1} h_r \bar{\alpha}^r$. The approach in determining parameters h_r is very similar to the procedure in determining c_{rj} in Step 1. Since h_r is determined assuming the solution is smooth, it is not suitable when the solution has a discontinuity in one or more of the candidate stencils. In this case we must turn off the weights for the stencils containing the discontinuities. We therefore use nonlinear weights w_r to replace h_r with a built in smoothness indicator so that $w_r = h_r + O(\Delta x^{p_2-1})$ in the smooth region, and it is automatically set to a small value close to 0 for stencils containing a discontinuity. Following the approach in [8], we

choose the following weights

$$w_r = \frac{\delta_r}{\sum_{r=0}^{k-1} \delta_r}, \quad \delta_r = \frac{h_r}{(\epsilon + \beta_r)^2}$$

$$\beta_r = \sum_{l=1}^{k-1} \int_{x_{i-1/2}}^{x_{i+1/2}} \Delta x^{2l-1} \left(\frac{\partial^l p_r(x)}{\partial^l x} \right)^2 dx, \quad r = 0, \dots, k-1 \quad (31)$$

where $p_r(x)$ is the polynomial of k th order over the interval $[x_{i-1/2}, x_{i+1/2}]$ determined by the given solutions on stencil $\{x_{i-r}, \dots, x_{i+s}\}$. The smoothness indicators are given in [1, 8, 19]. Performance tests with these smoothness indicators will be presented later. It will be shown that these weights are not suitable for short waves because they cannot distinguish short waves with 6 PPW from discontinuities. A new set of weights will be presented in a later section.

In this paper we constructed a variety of schemes with different stencil sizes, and order of accuracy. In our optimization, we have selected $\lambda = 0.5$ to minimize both the dissipation and dispersion errors and $\alpha_0 \Delta x = 0.35\pi$. The selection of $\alpha_0 \Delta x = 0.35\pi$ optimizes the schemes for waves with about 6 PPW. Figures 1-3 show the comparison of the relative wavenumber errors between the OWENO schemes of different order of accuracy and the 7th order accurate WENO scheme with the same stencil (without the smoothness indicators). Lele defines the resolving efficiency as the fraction of range of wave number such that the error is below some tolerance τ [10]. If the tolerance is set to be 0.01, then the resolving efficiency of the first-order OWENO scheme is $1.45/\pi = 0.46$ (corresponding to 4.3 PPW), the resolving efficiency of the third-order OWENO scheme is $1.46/\pi = 0.46$ (4.3 PPW), the resolving efficiency of the fifth-order OWENO scheme is $1.22/\pi = 0.39$ (5.2 PPW), and the resolving efficiency of the seventh-order WENO scheme is $1.25/\pi = 0.40$ (5.0 PPW). However if higher accuracy is required, e.g., $\tau = 0.001$, then the resolving efficiency of the first-order OWENO scheme is $1.15/\pi = 0.37$ (corresponding to 5.5 PPW), the resolving efficiency of the third-order OWENO scheme is $1.16/\pi = 0.37$ (5.5 PPW), the resolving efficiency of the fifth-order OWENO scheme is $0.82/\pi = 0.26$ (7.7 PPW), and the resolving efficiency of the seventh-order WENO scheme is $0.86/\pi = 0.27$ (7.3 PPW). It is interesting to see that the fifth-order OWENO scheme has a lower resolving efficiency than the maximum-order, non-optimized seventh-order WENO scheme. We could not understand why this is the case. On the other hand, the first-order and third-order OWENO schemes do have better resolving efficiency than the WENO scheme for $k = 4$. Since the third-order OWENO scheme has a higher formal order of accuracy, and a slightly better resolving efficiency, it is selected in all the numerical computations to be shown later.

Extension to the Linearized Euler Equations

The unsteady Euler equations in conservation form in quasi-1D can be written as:

$$\frac{\partial Q}{\partial t} + \frac{\partial F}{\partial x} = H \quad (32)$$

where Q is the vector of conserved variables, F is inviscid flux vectors in the x -direction, and H is the vector for the source terms given below

$$\begin{aligned} Q &= A\{\rho, \rho u, E\} \\ F &= A\left\{\rho u, \rho u^2 + p, u(E + p)\right\} \\ H &= \left\{0, p \frac{\partial A}{\partial x}, 0\right\} \end{aligned} \quad (33)$$

Here ρ is density, u is the velocity, p is the pressure, E is the total energy, A is the area of the cross section. Pressure is related to the total energy by

$$E = \frac{p}{\gamma - 1} + \frac{1}{2}\rho u^2. \quad (34)$$

with $\gamma = 1.4$ for air. The linearized Euler equations can be derived by letting

$$p = p_0 + p', \quad \rho = \rho_0 + \rho', \quad u = u_0 + u' \quad (35)$$

where the quantities with subscript 0 are the mean flow values, while those with ' are perturbations. Substituting (35) into (32), and eliminating high-order terms with respect to the perturbations, we obtain the linearized Euler equations. The linearized Euler equations can be written in two forms, one in conservation form, and the other in non-conservation form. The non-conservative linearized Euler equations in curvilinear coordinate $x = x(\xi)$ can be written as:

$$\frac{\partial q}{\partial t} + \left(J \frac{\partial q}{\partial \xi} \right) \frac{d\xi}{dx} = S \quad (36)$$

where $q = \{\rho', u', p'\}$, J is the Jacobian matrix, and S contains the vector of sources, which are functions of the mean flow variables, their first derivatives, and nozzle area derivatives. The OWENO scheme for equation (36) takes the following form:

$$\frac{\partial q_i}{\partial t} + \frac{1}{\Delta \xi} [J_i^+ (\tilde{q}_{i+1/2}^- - \tilde{q}_{i-1/2}^-) + J_i^- (\tilde{q}_{i+1/2}^+ - \tilde{q}_{i-1/2}^+)] \left(\frac{d\xi}{dx} \right)_i = S_i \quad (37)$$

Here each component of $\tilde{q}_{i+1/2}^-$ is computed using the procedure presented in the last section, which assumes that the wave travels in the positive x direction. Each component of $\tilde{q}_{i+1/2}^+$ is computed in a symmetric fashion assuming the wave travels in the negative x direction. The Jacobian matrix J can be decomposed into two parts, $J = J^+ + J^-$, with J^+ containing

only non-negative eigenvalues and J^- only non-positive eigenvalues. The following equation is used to decompose J :

$$\begin{aligned} J^+ &= \frac{1}{2} R_J (\Lambda_J + |\Lambda_J|) R_J^{-1} \\ J^- &= \frac{1}{2} R_J (\Lambda_J - |\Lambda_J|) R_J^{-1} \end{aligned}$$

where R_J is composed of the eigenvectors of J and Λ_J is a diagonal matrix including the eigenvalues of J .

Note that the non-conservative linearized Euler equations have the first derivatives of the mean flow in the source terms, which become singular if the mean flow has a discontinuity. To handle discontinuous mean flow, one must use the conservation form:

$$\frac{\partial U}{\partial t} + \frac{\partial G}{\partial x} = \Theta \quad (38)$$

where U is the conserved perturbation variables, G is the flux, and Θ is the source vector. Let the Jacobian matrix be B , then $B = \frac{\partial G}{\partial U}$. Now the source term does not contain the derivatives of mean flow variables. We seek a conservative finite-difference scheme in the form:

$$\frac{\partial U_i}{\partial t} + \frac{1}{\Delta x} \left(\tilde{G}_{i+\frac{1}{2}} - \tilde{G}_{i-\frac{1}{2}} \right) = \Theta(x_i) \quad (39)$$

Here \tilde{G} is a vector numerical flux function. Here we employ a component-wise, flux-splitting approach [19] to compute the numerical flux vector. The Lax-Friedrichs splitting is selected for its simplicity and smoothness. The left and right propagating flux vectors are defined by

$$G^- = 0.5[G - \max|\lambda^l|U] \quad G^+ = 0.5[G + \max|\lambda^l|U] \quad (40)$$

where λ^l , $l=1,2,3$ are the three eigenvalues of matrix B . Then the numerical flux vector is computed with

$$\tilde{G}_{i+1/2} = \tilde{G}_{i+1/2}^- + \tilde{G}_{i+1/2}^+ \quad (41)$$

Each component of $G_{i+1/2}^{r,-}$ and $G_{i+1/2}^{r,+}$ are computed

based on G^- and G^+ all the candidate stencil $\{x_{i-r}, \dots, x_{i+s}\}$ using either the maximum order or optimized schemes. The convex combination of $G_{i+1/2}^{r,-}$ or $G_{i+1/2}^{r,+}$ for all candidate stencils can also be obtained by the procedure given in the previous section.

For the inlet and exit boundary conditions, we following the approach developed in [21]. Interested readers should consult [21] for details. One-sided optimized schemes are used to maintain the solution accuracy near boundaries.

Time-Integration

Up to now, we have only considered spatial discretizations, leaving the time derivative continuous. After proper spatial discretizations, the conservation laws reduce to either a scalar or a system of ordinary differential equations in time, which can be written in the form:

$$\frac{dQ}{dt} = L(Q) \quad (42)$$

In this study which time-discretization is not a major concern, the high-order TVD Range-Kutta methods developed in [18] are employed. A general m -stage Runge-Kutta method for equation (42) can be written in the following form

$$Q^{(j)} = \sum_{l=0}^{j-1} \left(\alpha_{jl} Q^{(l)} + \Delta t \beta_{jl} L(Q^{(l)}) \right), \quad j = 1, \dots, m \quad (43)$$

with $Q^{(0)} = Q^n$ and $Q^{n+1} = Q^{(m)}$. Where Δt is the time step and n is the time level, α_{jl} and β_{jl} are constant coefficients. The optimal third order TVD given in [19] will be used in this study. The optimal third-order TVD Range-Kutta scheme is given by:

$$\begin{aligned} Q^{(1)} &= Q^n + \Delta t L(Q^n) \\ Q^{(2)} &= \frac{3}{4} Q^n + \frac{1}{4} Q^{(1)} + \frac{1}{4} \Delta t L(Q^{(1)}) \\ Q^{n+1} &= \frac{1}{3} Q^n + \frac{2}{3} Q^{(2)} + \frac{2}{3} \Delta t L(Q^{(2)}) \end{aligned} \quad (44)$$

Test with Linear Wave Equation and New Smoothness Indicators

To verify the designed advantages of OWENO schemes, we first tested WENO and OWENO schemes for the linear wave equation (1) with $a = 1$. In all of our computations, we used the third order accurate TVD Runge-Kutta method for time integration [18,19]. In the first case a sine wave

$u_0(x) = \sin\left(\frac{\pi}{3}x\right)$ was specified in the computational domain

and propagated with periodic boundary conditions. We initially turned off the ‘‘smoothness indicators’’ in both WENO and OWENO schemes since the solution was smooth. The computational domain for this case was set to be $[-18, 18]$ with grid size $\Delta x = 1$, i.e., 6 PPW. The time step was set at $\Delta t = 0.1$ to minimize the effects (if any) of the time-integration scheme. The simulation was then carried out until $t = 60$. By then, the sine wave traveled for 10 wave lengths. Figure 4a shows the comparison of the solutions with the WENO and OWENO schemes to the exact solution. The solution errors are compared in Figure 4b. Note that the

solution error obtained with OWENO is significantly lower (by more than an order of magnitude) than that with WENO. Next, we turned on the smoothness indicators with everything else remaining exactly the same. The solutions with both WENO and OWENO schemes are compared to the exact solution in Figure 5a, and the solution errors are shown in Figure 5b. Again, the solution error with OWENO is significantly lower than that with WENO. However, the errors with both schemes are significantly higher than those without smoothness indicators. This case clearly indicates that the smoothness indicators ‘‘thought’’ that the sine wave at 6 grid-spacings per-wave was actually discontinuous, and therefore were turned on. Therefore, significant numerical dampings were added in the solution, as is evident in Figure 5. If we are to develop proper OWENO schemes for short waves, it is critical that the smoothness indicators should not be turned on for short waves. We tested a variety of new smoothness indicators, and found the following one works the best for short waves

$$\beta_r = \sum_{l=k-2}^{k-1} \left[\int_{x_{i-1/2}}^{x_{i+1/2}} \Delta x \frac{\partial^l p_r(x)}{\partial^l x} dx \right]^2, \quad r = 0, \dots, k-1 \quad (45)$$

For $k = 4$, the new smoothness indicators take the following form:

$$\begin{aligned} \beta_0 &= (2u_i - 5u_{i+1} + 4u_{i+2} - u_{i+3})^2 + (-u_i + 3u_{i+1} - 3u_{i+2} + u_{i+3})^2 \\ \beta_1 &= (u_{i-1} - 2u_i + u_{i+1})^2 + (-u_{i-1} + 3u_i - 3u_{i+1} + u_{i+2})^2 \\ \beta_2 &= (u_{i-1} - 2u_i + u_{i+1})^2 + (-u_{i-2} + 3u_{i-1} - 3u_i + u_{i+1})^2 \\ \beta_3 &= (-u_{i-3} + 4u_{i-2} - 5u_{i-1} + 2u_i)^2 + (-u_{i-3} + 3u_{i-2} - 3u_{i-1} + u_i)^2 \end{aligned}$$

With the new smoothness indicators, the solutions with WENO and OWENO and their errors are shown in Figure 6. It is obvious that the solution errors with the new smoothness indicators are reduced significantly comparing to those with the original smoothness indicators. The solution errors with and without the smoothness indicators are presented in Figure 7. Note that the new smoothness indicators do not significantly affect the short waves for both WENO and OWENO schemes. The performance of the new smoothness indicators for discontinuities will be shown later. Next, the OWENO scheme was tested for an artificial ‘‘broadband’’ wave which is composed of the following three sine waves as given by

$$u_0(x) = \sin\left(\frac{\pi x}{3}\right) + \sin\left(\frac{\pi x}{6}\right) + \sin\left(\frac{\pi x}{12}\right)$$

The wave lengths of the three waves are 6, 12 and 24 respectively, and they are therefore called short, medium and long waves. The initial wave form is displayed in Figure 8. Because WENO and OWENO schemes are strongly non-linear, the solution for this ‘‘broadband’’ wave with WENO and OWENO schemes does not equal to the summation of the solutions for each separate wave. The computational domain was chosen to be $[-12, 12]$ with grid size $\Delta x = 1$ and $\Delta t = 0.1$.

The wave then traveled for 5 short wave lengths until $t = 30$. The solutions with WENO and OWENO schemes are compared with the exact solution in Figure 9a. The solution errors are shown in Figure 9b. Again OWENO performed better than WENO as expected for this artificial ‘‘broadband’’ wave. After that, we wanted to see how OWENO schemes perform for discontinuities. In this test, a square wave was propagated in the computational domain with periodic boundary conditions. The computational domain was chosen to be $[-30, 30]$ with $\Delta x = 0.5$. The initial wave was specified as

$$u_0 = \begin{cases} 1 & -10 \leq x \leq 10 \\ 0 & \text{otherwise} \end{cases}$$

The time step Δt was set to 0.1, which is small enough so that the error due to time integration is negligible. The simulation was carried out until $t = 120$. Therefore, the wave was allowed to travel across the computational domain twice. Figure 10 shows the numerical results with WENO and OWENO using the new smoothness indicators and the exact solution. Note that both WENO and OWENO gave monotonic solutions for the square wave (at least to the naked eyes) although OWENO smeared the solution slightly more than WENO. This case also demonstrates that the new smoothness indicators work well for discontinuities. Just to show the comparison between the new and original smoothness indicators for discontinuities, we used both smoothness indicators with the WENO scheme to perform the same simulation. Figure 11 displays the solutions with the original and new smoothness indicators. The solutions are indistinguishable from each other. Finally to demonstrate the

potential of OWENO schemes for shock/acoustic wave interaction problems, the linear combination of a square wave and a sine wave was simulated. The period of the combined wave was 24. The initial wave form was set to be

$$u_0 = \begin{cases} 1 + \sin\left(\frac{\pi x}{3}\right), & 7.5 \leq x < 19.5 \\ \sin\left(\frac{\pi x}{3}\right) & \text{otherwise} \end{cases}$$

which is displayed in Figure 12. The computational domain for the case was $[0, 24]$ with $\Delta x = 1$ and $\Delta t = 0.1$. The simulation was carried out until $t = 48$ so that the wave traveled across the computational domain twice. The computed solutions with WENO and OWENO schemes are shown in Figure 13. Although both schemes smeared the discontinuity heavily at this grid resolution, it is noted that the smearing of the discontinuity does not affect the resolution of the sine wave that much with the OWENO scheme. For the WENO scheme, however, the resolution for the sine wave is much lower. In practical CAA simulations involving discontinuities, it may not always be possible to resolve the discontinuities with high-resolutions. With OWENO schemes, it seems hopeful that the

acoustic waves may still be resolved with high resolutions.

Application to CAA Benchmark Problems

After the advantages of OWENO schemes were verified on the linear wave equation, they were then extended to solve the linearized Euler equations, in both the conservation and non-conservation forms. Two benchmark problems from the Third Computational Aeroacoustics (CAA) Workshop on Benchmark Problems [22] were then solved with the OWENO schemes. For both problems the third order TVD Runge-Kutta method was employed for time integration.

Problem 1: Propagation of Sound Waves through a Transonic Nozzle

This benchmark problem is designed to model acoustic wave propagation through a nozzle where the local Mach number near the throat may be close to 1. The area variation of the nozzle is given by

$$A(x) = \begin{cases} 0.536572 - 0.198086e^{-\ln 2 \left(\frac{x}{0.6}\right)^2}, & x > 0 \\ 1.0 - 0.661514e^{-\ln 2 \left(\frac{x}{0.6}\right)^2}, & x < 0 \end{cases} \quad (46)$$

The governing equations are the linearized quasi-1D Euler equations. The Mach number in the uniform region downstream of the throat is 0.4. Small amplitude acoustic waves, with angular frequency $\omega = 0.6\pi$, is generated way downstream and propagate upstream through the narrow passage of the nozzle throat. The upstream-propagating wave in the uniform region downstream of the nozzle throat is represented by

$$\begin{bmatrix} \rho' \\ u' \\ p' \end{bmatrix} = \mu \begin{bmatrix} 1 \\ -1 \\ 1 \end{bmatrix} \cos\left[\omega\left(\frac{x}{1-M} + t\right)\right] \quad (47)$$

where $\mu = 10^{-5}$. The computational domain is $[-10, 10]$. Since the mean flow was smooth, the non-conservation form linearized Euler equations were used in the simulation. A non-uniform grid with 301 points was employed with a hyperbolic sine transformation. The grid was clustered near the throat, and the ratio between the largest grid spacing to the smallest was about 30. The mean flow was computed analytically. No smoothness indicators were used in the weights because of the smooth mean flow. The time step was set to be 0.005. The simulation started with zero perturbations everywhere until it reached a periodic state-state. Figure 14 displays the exact maximum pressure envelope and the computed pressure distributions at four different times in a period. It is obvious that the pressure distributions are nicely bounded by, and touch the exact envelope. The computed pressure envelope is then compared with the exact pressure envelope in Figure 15. Enlarged views of the same Figure near the throat and exit are

shown in Figure 16. Note that the agreement between the computational and exact solutions is excellent.

Problem 2: Shock-Sound Interaction

This problem is designed to simulate shock-sound interactions. The geometry is exactly the same as in Problem 1, but now there is a supersonic shock downstream of the throat. The inlet Mach number is $M = 0.2006533$, and the exit pressure is set at 0.6071752 to generate a normal shock downstream of the throat. At the inflow boundary, the conditions are:

$$\begin{bmatrix} \rho \\ u \\ p \end{bmatrix} = \begin{bmatrix} 1 \\ M \\ \frac{1}{\gamma} \end{bmatrix} + \mu \begin{bmatrix} 1 \\ 1 \\ 1 \end{bmatrix} \sin \left[\varpi \left(\frac{x}{1+M} - t \right) \right] \quad (48)$$

where $\mu = 10^{-5}$, $\varpi = 0.6\pi$. Since there was a shock wave in the mean flow, we employed the conservation-form linearized Euler equations. The mean flow was again obtained analytically, and is shown in Figure 17. A uniform grid with 201 points in the computational domain $[-10, 10]$ was used. A time step of 0.01 was employed in the simulation. We again started the simulation from zero perturbation fields everywhere until the computation reached a periodic steady state. Figure 18 shows the comparison of the computed pressure field using OWENO and the exact pressure solution at the beginning of a period. Note that the agreement between the computational and exact pressure fields is excellent before and after the shock wave. There is, however, a slight oscillation near the shock wave in the computed field. This could be due to several factors. One possible factor is that the extension of the scalar scheme to the linearized Euler equations is done using a split flux approach. An extension based on the characteristic variables may give better predictions near the shock. Furthermore the smoothness indicators may still not be the most suitable for the optimized schemes for the linearized Euler equations. Future work is necessary to investigate the cause of the oscillations around the shock wave. Just for comparison purposes, we also used the non-conservative linearized Euler equations to simulate this case assuming that the shock wave is smeared over one mesh spacing so that finite first derivatives of the mean flow can be calculated. The computed pressure field using the non-conservative linearized Euler equations is compared to the exact solution in Figure 19. Note that the acoustic wave was heavily damped when it passed the shock. Ahead of the shock, the agreement between the computational and exact solutions is very good. Finally the computed pressures at the exit over a period using both the conservative and non-conservative linearized Euler equations are compared with the exact solution in Figure 20. The conservative form gave an excellent prediction while the non-conservative produced a heavily damped solution. This simulation demonstrates the importance of conservation in the computational simulations with discontinuities.

Conclusions

Optimized weighted ENO schemes have been developed in this study to unite the advantages of both the optimized and WENO schemes in the simulation of shock/broadband acoustic waves. By design, OWENO schemes are capable of resolving waves at 6 PPW, while giving essentially non-oscillatory solutions for discontinuities. Two levels of optimizations can be performed in OWENO schemes. First optimized schemes for all candidate stencils (given a stencil size) are constructed to minimize the solution error in the wave number space. Then these optimized schemes are convexly combined with weights optimized to achieve both higher-order of accuracy and better resolution for short waves. Smoothness indicators are built in the weights to essentially turn off the contributions made by stencils containing discontinuities. It was found that the original smoothness indicators [8] added significant numerical dampings into the schemes for waves at 6 PPW. New smoothness indicators are developed, and shown to perform much better for waves at 6 PPW. These smoothness indicators also were tested with discontinuities, and were found to perform as well as the original indicators. Numerical tests with the scalar model wave equation verified the designed advantages of OWENO schemes. The OWENO schemes are then extended to the linearized Euler equations, in both the conservation and non-conservation forms. Two problems in the Third Computational Aeroacoustics (CAA) Workshop on Benchmark Problems were solved with the third order OWENO scheme. The scheme was found to perform very satisfactorily for both problems. It is shown, however, the conservation form linearized Euler equations must be used if the mean flow is discontinuous to capture the proper behavior of the acoustic waves across the shock wave. The OWENO schemes are ideally suited to solve the non-linear Euler equations for shock-acoustic wave interaction, shock-vortex interaction and shock/turbulence interaction problems. The implementation of the OWENO schemes for the non-linear Euler equations is now under way, and will be reported in a future publication.

Acknowledgments

The authors want to thank Dr. C.-W. Shu for bringing [1] and [24] to their attention. We also acknowledge helpful discussions with Dr. C.-W. Shu and Dr. D.S. Balsara on smoothness indicators.

References

1. D.S. Balsara and C.-W. Shu, Monotonicity preserving weighted essentially non-oscillatory schemes with increasingly high-order accuracy, *J. Comput. Phys.* **160**, 405-452 (2000).
2. J. Casper and H.L. Atkins, A finite volume high-order ENO scheme for two-dimensional hyperbolic systems, *J.*

Comput. Phys. **106**, 62-76 (1993).

3. D. Gaitonde and J.S. Shang, Optimized compact-difference-based finite volume schemes for linear wave phenomena, *J. Comput. Phys.* **138**, 617-647 (1997).
4. A. Harten, High resolution schemes for hyperbolic conservation laws, *J. of Comput. Phys.* **49**, 357-393 (1983).
5. A. Harten, B. Engquist, S. Osher and S. Chakravarthy, Uniformly high order essentially non-oscillatory schemes III, *J. Comput. Phys.* **71**, 231 (1987).
6. R. Hixon, Evaluation of a high-accuracy MacCormack-type scheme using benchmark problems, NASA Contractor Report 202324, ICOMP-97-03, 1997.
7. A. Jameson, W. Schmidt and E. Turkel, Numerical solutions of the Euler equations by finite volume methods using Range-Kutta time-stepping, AIAA Paper No. 81-1259, 1981.
8. G. Jiang and C.-W. Shu, Efficient implementation of weighted ENO schemes, *J. Comput. Phys.* **126**, 202 (1996).
9. C. Kim, P.L. Roe and J.P. Thomas, Accurate schemes for advection and aeroacoustics, AIAA Paper No. 97-2091, 1997.
10. S.K. Lele, Compact finite difference schemes with spectral-like resolution, *J. Comput. Phys.* **103**, 16-42 (1992).
11. S. Y. Lin and Y.S. Chin, Comparison of higher resolution Euler schemes for aeroacoustics computations, *AIAA J.* **33**, 237-245 (1995).
12. X.D. Liu, S. Osher and T. Chan, Weighted essentially non-oscillatory schemes, *J. Comput. Phys.* **115**, 200-212 (1994).
13. Y. Liu, Fourier analysis of numerical algorithms for the Maxwell equations, *J. Comput. Phys.* **124**, 396-416 (1996).
14. D.P. Lockard, K.S. Brentner and H.L. Atkins, High-accuracy algorithms for computational aeroacoustics, *AIAA J.* **33**, 246-251 (1995).
15. S. Osher and S. Chakravarthy, Upwind schemes and boundary conditions with applications to Euler equation in general geometries, *J. Comput. Phys.* **50** 447-481 (1983) .
16. P.L. Roe, Approximate Riemann solvers, parameter vectors, and difference schemes, *J. Comput. Phys.* **43** 357-372 (1981).
17. L.N. Sankar, N.N. Reddy and N. Hariharan, A third order upwind scheme for aeroacoustic application, AIAA Paper No. 93-0149, 1993.
18. C.-W. Shu, Total-Variation-Diminishing time discretizations, *SIAM Journal on Scientific and Statistical Computing* **9**, 1073-1084 (1988).
19. C.-W. Shu, Essentially non-oscillatory and weighted essentially non-oscillatory schemes for hyperbolic conservation laws, ICASE Report 97-65, 1997.
20. C.K.W. Tam, Computational aeroacoustics: issues and methods," *AIAA J.* **33**, 1788-1796 (1995).
21. C.K.W. Tam and J.C. Webb, Dispersion-relation-preserving finite difference schemes for computational acoustics, *J. Comput. Phys.* **107**, 262-281, (1993).
22. C.K.W. Tam, L.N. Sankar and D.L. Huff, Third

Computational Aeroacoustics (CAA) Workshop on Benchmark Problems, 8-10 November, 1999, Cleveland, Ohio.

23. B. van Leer, Towards the ultimate conservative difference scheme V. a second order sequel to Godunov's method, *J. Comput. Phys.* **32**, 101-136 (1979).
24. V.G. Weirs and G.V. Candler, Optimization of weighted ENO schemes for DNS of compressible turbulence, AIAA Paper No. 97-1940, 1997.
25. M. Zhuang and R.F. Chen, Optimized upwind dispersion-relation-preserving finite difference schemes for computational aeroacoustics." *AIAA J.* **36**, 2146 (1998).
26. M. Zhuang and R.F. Chen, Applications of the optimized upwind dispersion relation preserving schemes for multi-dimensional acoustic problems." AIAA Paper No. 98-2367, 1998.
27. D.W. Zingg, A review of high-order and optimized finite-difference methods for simulating linear wave phenomena, AIAA Paper No. 97-2088, 1997.

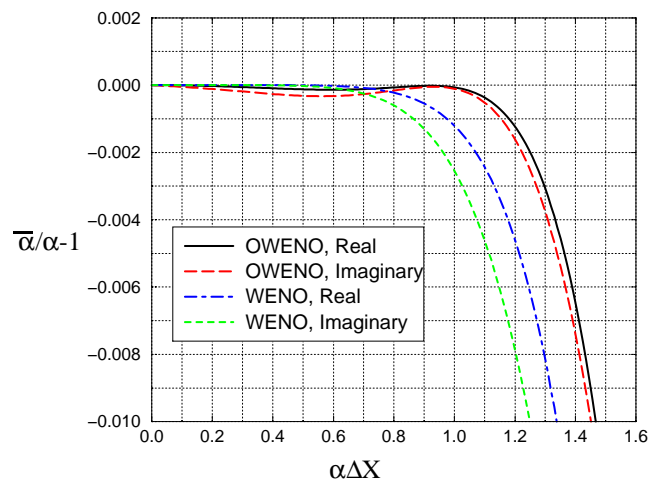


Figure 1. Comparison of Relative Wavenumber Errors between the Seventh-Order WENO Scheme and the First-Order OWENO Scheme with $p_1 = 1$, and $p_2 = 0$.

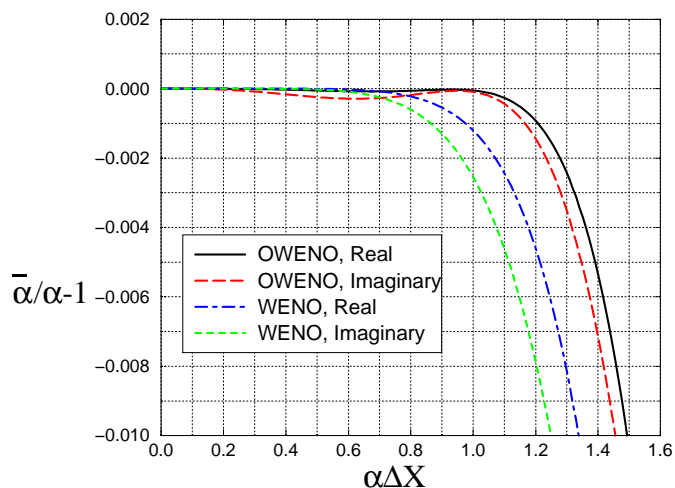


Figure 2. Comparison of Relative Wavenumber Errors between the Seventh-Order WENO Scheme and the Third-Order OWENO Scheme with $p_1 = 2$, and $p_2 = 1$.

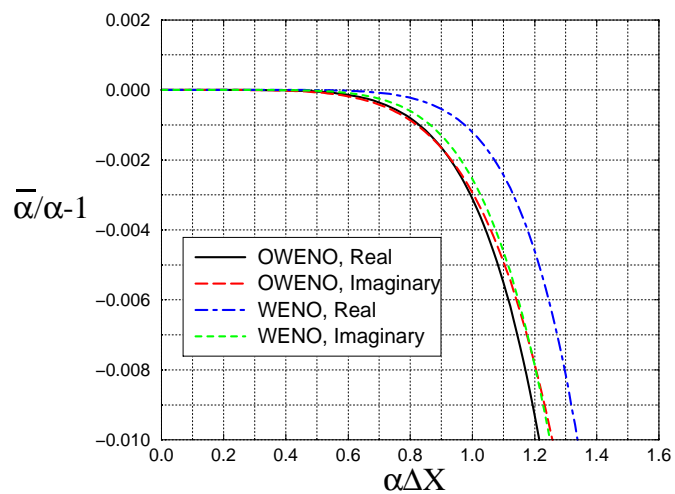


Figure 3. Comparison of Relative Wavenumber Errors between the Seventh-Order WENO Scheme and the Fifth-Order OWENO Scheme with $p_1 = 3$, and $p_2 = 2$.

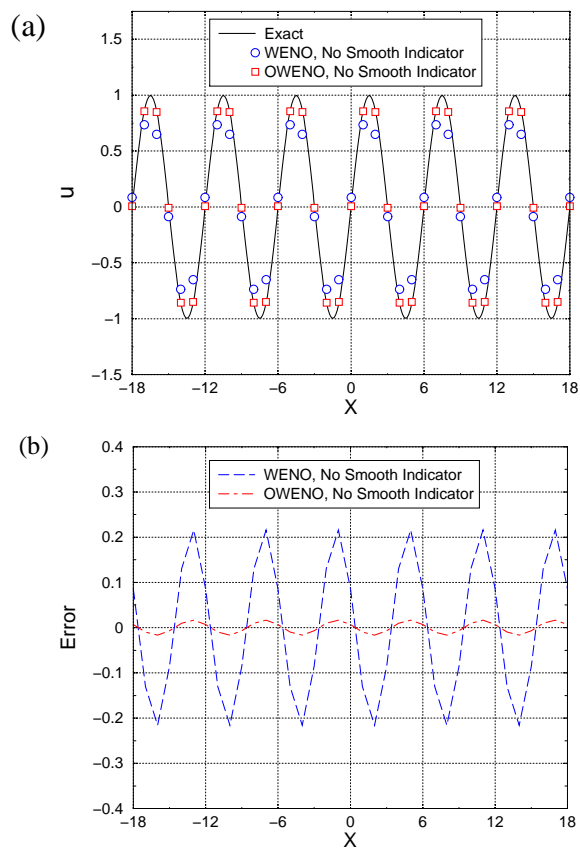


Figure 4. Comparison of WENO and OWENO Schemes for the Propagation of a Sine Wave without the Smoothness Indicators

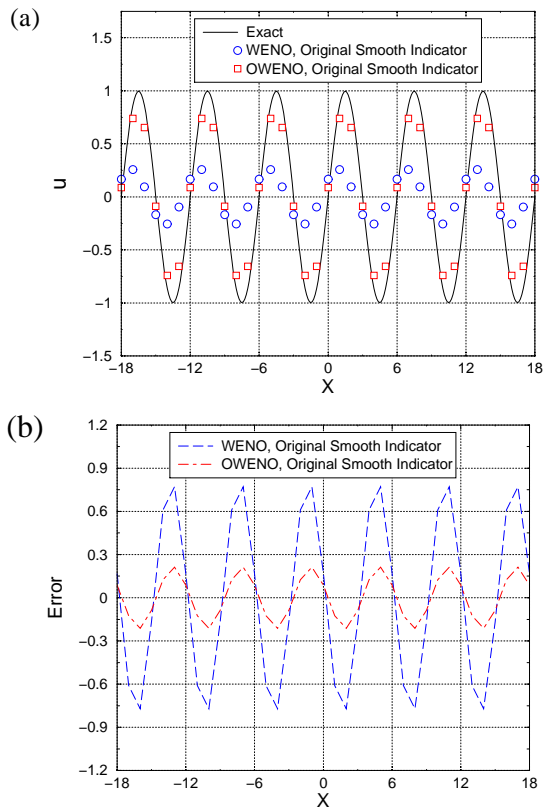


Figure 5. Comparison of WENO and OWENO Schemes for the Propagation of a Sine Wave with the Original Smoothness Indicators in [8]

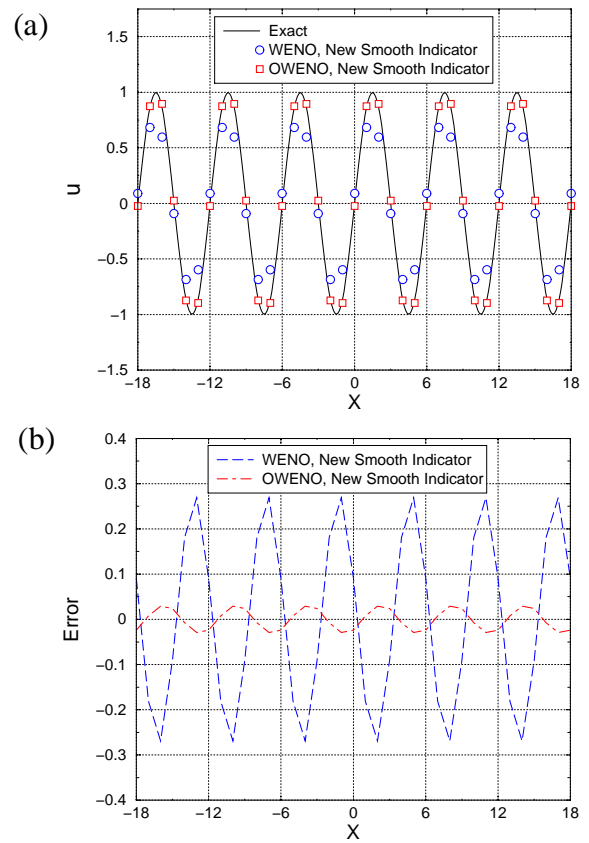


Figure 6. Comparison of WENO and OWENO Schemes for the Propagation of a Sine Wave with the New Smoothness Indicators

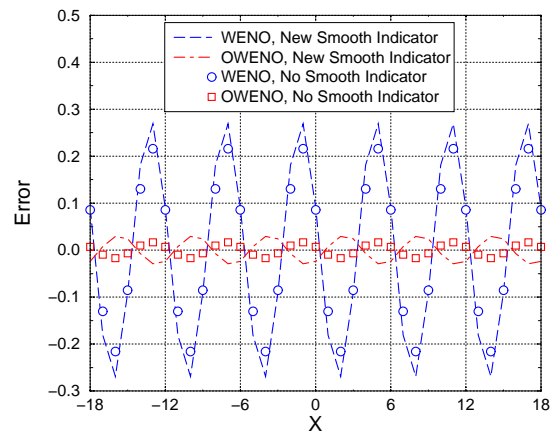


Figure 7. Comparison of WENO and OWENO Schemes for the Propagation of a Sine Wave with the New Smoothness Indicators and without Smoothness Indicators

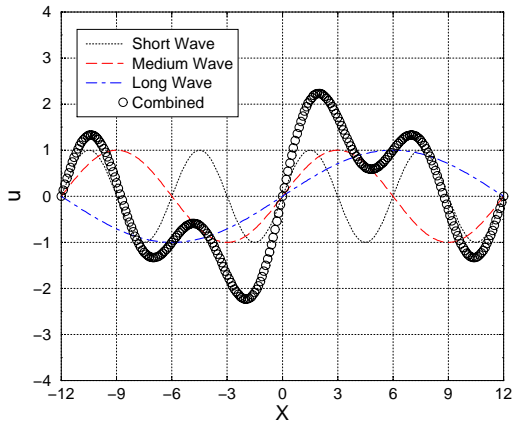


Figure 8. The Formation of a “Broadband” Wave

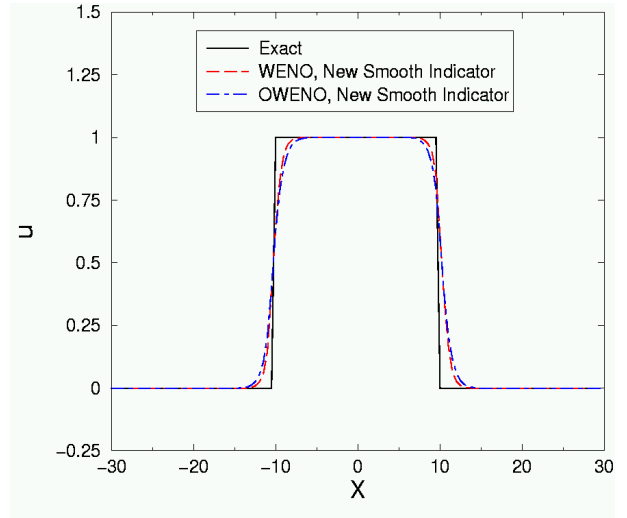


Figure 10. Comparison of WENO and OWENO Schemes for the Propagation of a Square Wave with the New Smoothness Indicators

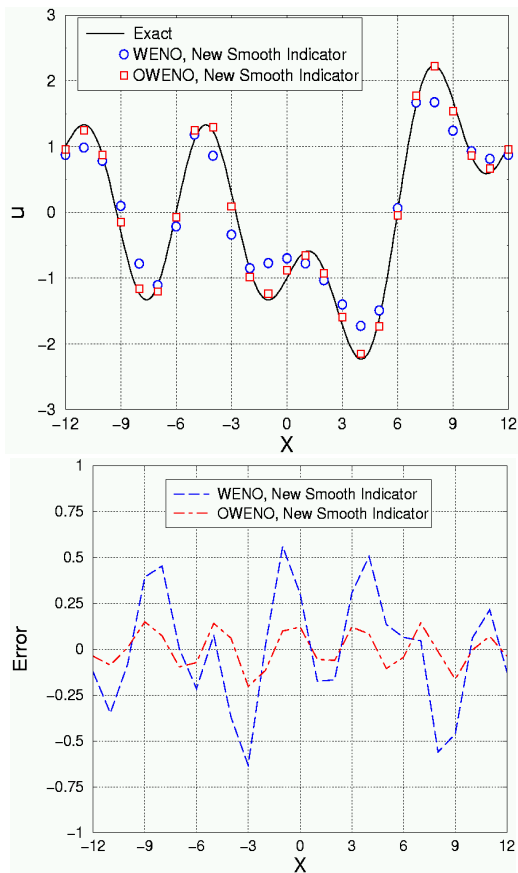


Figure 9. Comparison of WENO and OWENO Schemes for the Propagation of a “Broadband” Wave with the New Smoothness Indicators

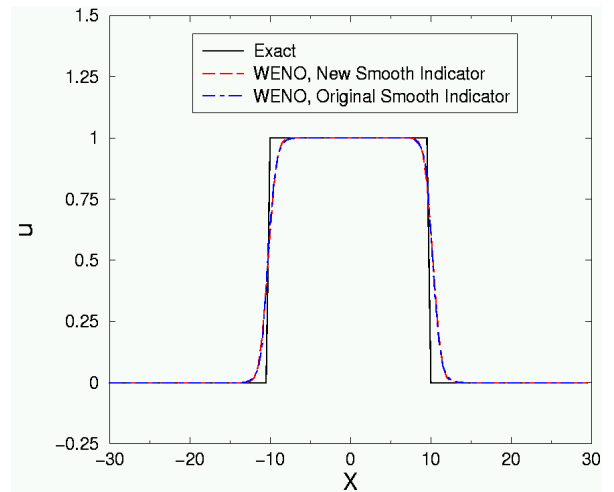


Figure 11. Comparison of WENO Schemes for the Propagation of a Square Wave with the Original and New Smoothness Indicators

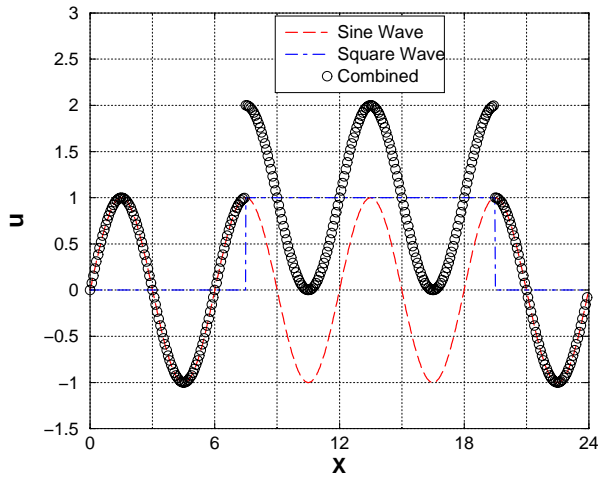


Figure 12. The Formation of a Discontinuous Sine Wave

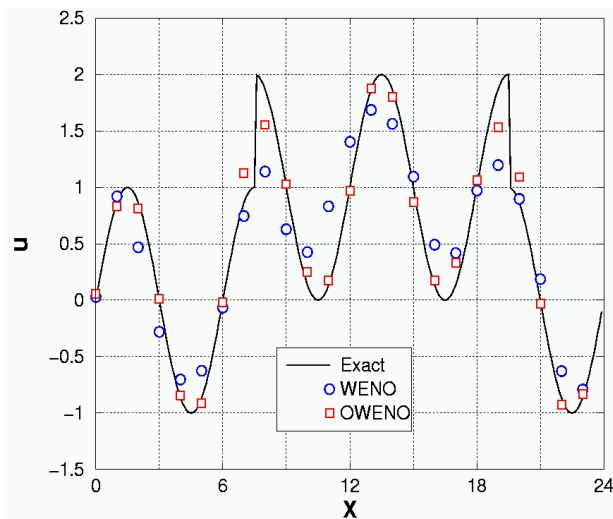


Figure 13. Comparison of WENO and OWENO Schemes for the Propagation of a Discontinuous Sine Wave with the New Smoothness Indicators

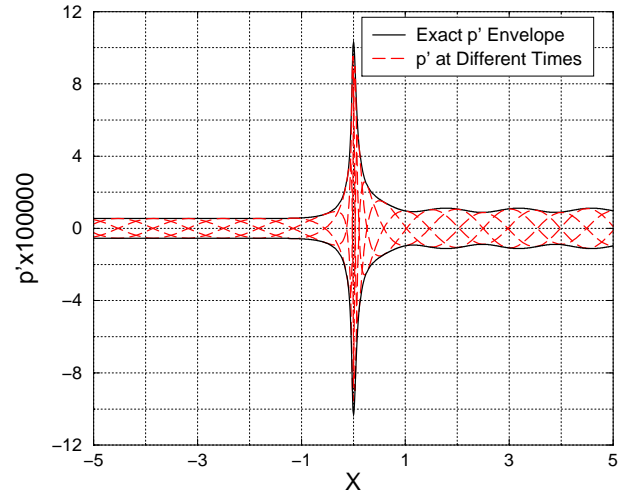


Figure 14. Comparison between the Exact Pressure Envelope and Computed Pressure Distributions at Four Different Times

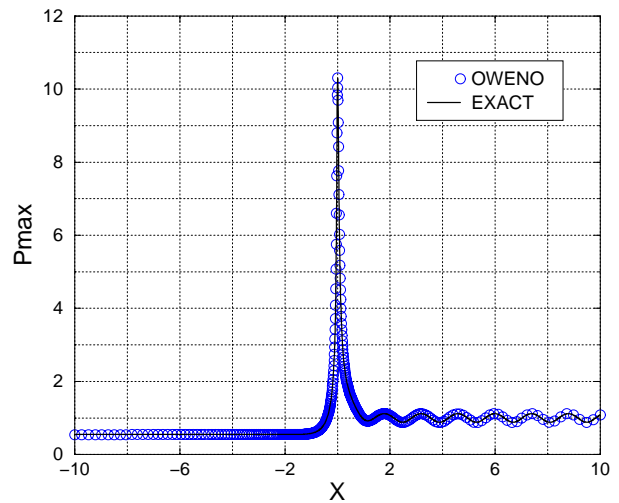


Figure 15. Comparison between the Exact Pressure Envelope and the Computed Pressure Envelope

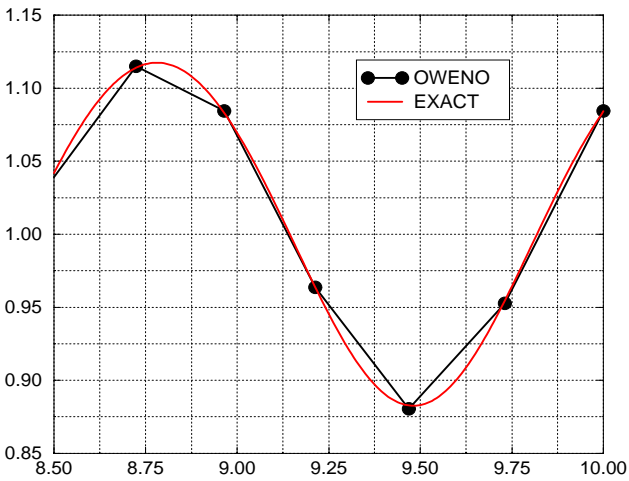
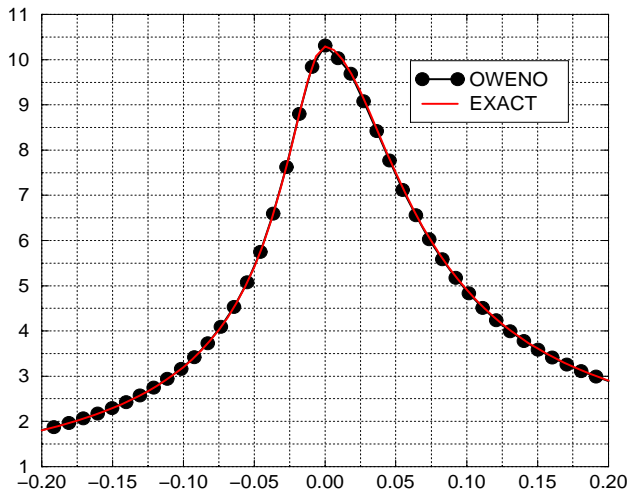


Figure 16 Comparison of the Computed Pressure Envelope and the Exact Pressure Envelope near the Throat and the Exit

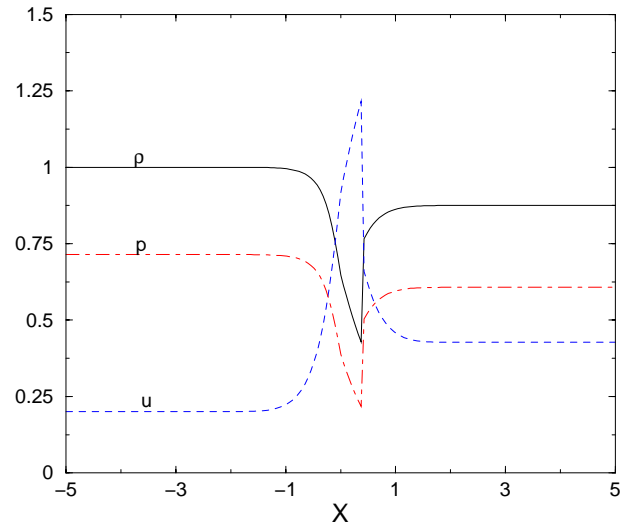


Figure 17. Mean Flow Distributions for Shock-Sound Interaction

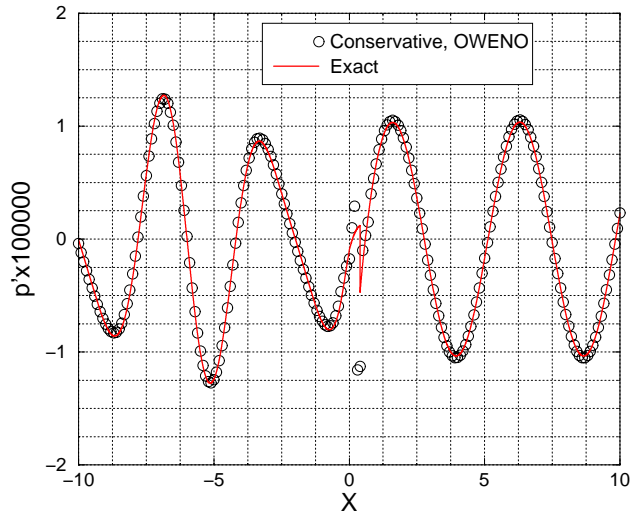


Figure 18. Comparison of Computed Pressure Distribution and Exact Solution at the Beginning of a Period Using the Conservation-Form Linearized Euler Equations

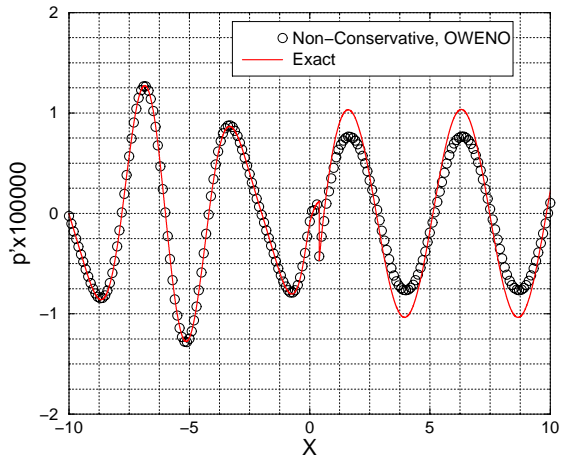


Figure 19. Comparison of Computed Pressure Distribution and Exact Solution at the Beginning of a Period Using the Non-Conservation-Form Linearized Euler Equations

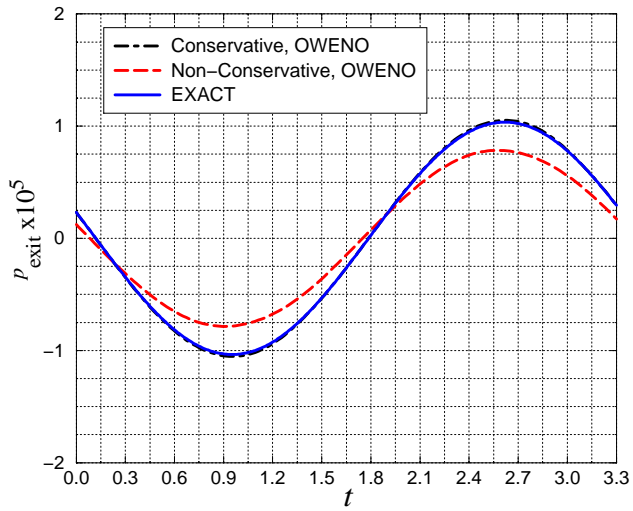


Figure 20. Comparison of the Computed Pressures and Exact Solution at the Exit for One Period